Thermochemical Properties of High Entropy Oxides Used as Redox-Active Materials in Two-Step Solar Fuel Production Cycles

Alex Le Gal, Marielle Vallès, Anne Julbe, Stéphane Abanades

catalysts

MDPI

Article

Thermochemical Properties of High Entropy Oxides Used as Redox-Active Materials in Two-Step Solar Fuel Production Cycles

Alex Le Gal [1], Marielle Vallès [2], Anne Julbe [2] and Stéphane Abanades [1,*]

[1] Processes, Materials and Solar Energy Laboratory (PROMES-CNRS), 7 rue du Four Solaire, 66120 Odeillo Font-Romeu, France

[2] Institut Européen des Membranes (IEM), CNRS, ENSCM, Université de Montpellier, Place Eugène Bataillon, 34095 Montpellier, France

* Correspondence: stephane.abanades@promes.cnrs.fr

Abstract: The main challenges and obstacles to the development of hydrogen/carbon monoxide production from the splitting of water/carbon dioxide through two-step solar thermochemical cycles are strongly related to material concerns. Indeed, ceria is the main benchmark redox material used in such processes because it provides very good oxidation reaction kinetics, reactions reversibility and thermal cycling stability. This is at the expense of a low reduction yield (non-stoichiometry δ in $CeO_{2-\delta}$) at relatively high temperatures (≥1400 °C), which requires operation at low oxygen partial pressures during the reduction step. Hence, the specific fuel output per mass of redox material, i.e., the amount of H_2/CO produced per cycle, remains low, thereby limiting the overall solar-to-fuel conversion efficiency. Perovskites offer larger amounts of fuel produced per cycle but the reaction kinetics are slow. This study addresses the thermochemical investigation of a new class of metal oxides, namely high entropy oxides (HEOs), with the aim of improving the specific amount of fuel generated per cycle with good kinetic rates. Different formulations of high entropy oxides were investigated and compared using thermogravimetric analysis to evaluate their redox activity and ability to split CO_2 during thermochemical cycles. Among the different formulations tested, five HEOs yielded CO with a maximum specific fuel output of 154 μmol/g per cycle. These materials' performances exceeded the production yields of ceria under similar conditions but are still far from the production yields reached with lanthanum–manganese perovskites. This new class of materials, however, opens a wide path for research into new formulations of redox-active catalysts comparing favorably with the ceria redox performance for solar thermochemical synthetic fuel production.

Keywords: hydrogen; water splitting; CO_2 conversion; thermochemical cycles; concentrated solar energy; high entropy oxides; redox materials; solar fuels

Citation: Le Gal, A.; Vallès, M.; Julbe, A.; Abanades, S. Thermochemical Properties of High Entropy Oxides Used as Redox-Active Materials in Two-Step Solar Fuel Production Cycles. *Catalysts* **2022**, *12*, 1116. https://doi.org/10.3390/catal12101116

Academic Editor: Gianluca Landi

Received: 26 August 2022
Accepted: 22 September 2022
Published: 26 September 2022

1. Introduction

Hydrogen is an energy vector that will play an important role in the future worldwide energy mix, as evidenced in the recent public policies of different countries [1–3]. Current production paths cannot be considered as sustainable solutions, because most of the hydrogen produced arises from the steam methane reforming process which emits large amounts of CO_2. Hence, hydrogen must be produced from renewable energy sources and new efficient processes have to be deployed. Converting solar energy into hydrogen and synthetic fuels is a promising pathway. Among the different possibilities, hydrogen can be produced from water electrolysis with electricity coming from photovoltaic modules or from photochemical processes, however, these two options face limited theoretical energy conversion (photons to hydrogen) efficiencies. Alternatively, the

thermochemical conversion of solar energy into hydrogen or synthetic fuels offers a higher theoretical conversion efficiency by directly using the heat generated by concentrated solar radiations in high-temperature thermochemical reactions [4]. Such a thermochemical process offers a thermodynamically favorable pathway for fuel production because it exploits the entire solar spectrum as the high-temperature process heat source to perform the thermochemical conversion. Two-step thermochemical cycles for splitting H_2O and CO_2 were extensively investigated for the last two decades, resulting in the development of advanced processes [5,6] and complete techno-economic analyses [7,8]. This production path first consists of the thermal activation of metal oxides (M_xO_y). During this first step, the metal oxide is thermally reduced (totally or partially) by releasing oxygen (Equation (1)). Then, during the second step, the reduced oxide reacts with steam (or CO_2) to be regenerated and produce hydrogen (or CO) (Equation (2)).

$$M_xO_y \rightarrow M_xO_{y-\delta} + \delta/2O_2 \quad (1)$$

$$M_xO_{y-\delta} + \delta H_2O \text{ (or } CO_2) \rightarrow M_xO_y + \delta H_2 \text{ (or CO)} \quad (2)$$

Two-step thermochemical cycles were initially proposed to reduce the temperature of the water-splitting reaction down to ~1400 °C—compared to direct thermolysis which requires at least 2500–3000 °C. Furthermore, such cycles do not require any material consumption (except water or CO_2 as reactants) because the oxide is entirely recycled (it thus acts as a redox catalyst), and they avoid any gas separation problems because O_2 and H_2 (or CO) are released in separate steps. The solar energy input is only necessary during the first reduction step to activate the intermediate redox material (creation of oxygen vacancies reflected by the sub-stoichiometry δ) because it is an endothermal reaction, whereas the second oxidation step is exothermal. Hence, the higher the temperature of the reduction step, the higher the reduction yield; conversely, the lower the temperature of the oxidation step, the higher the H_2 or CO production. A high theoretical conversion efficiency (solar-to-fuel) can be reached because this process involves a direct conversion of concentrated solar heat into fuel without any intermediate conversion limitations linked to the solar electricity production required for the electrolysis process.

However, a scientific barrier is still blocking the competitiveness of such processes, delaying deployment at an industrial scale. This barrier is related to material science and more precisely to the catalytic redox activity of reactive materials. Indeed, the solar fuel production cost is strongly dependent on the metal oxide performance that determines both the fuel production capacity (in mol per gram of oxide) and the reaction kinetics (fuel production rates in mol per gram per second). Explicitly, the higher the material reactivity in both redox steps is, the higher the fuel production output obtained per cycle; and the faster the reaction kinetics, the higher the number of cycles performed per day. Both aspects affect the global fuel production capacity of the process. As the material is cycled several times per day during the overall lifetime of the production plant, the material redox performance is crucial. Current state-of-the-art materials that appear to be the most suitable for solar-driven thermochemical hydrogen and fuel production are nickel ferrites ($NiFe_2O_4$) [9–12], cerium oxide (CeO_2) [13–21] and lanthanum manganite perovskites ($(La,Sr)MnO_3$) [22–28]. However, these materials suffer, respectively, from deactivation during cycling which is largely due to sintering [29], a low amount of fuel produced per cycle [30,31] and slow oxidation kinetics [32,33]. This is the reason why intense research efforts to discover a new class of materials that could overcome this scientific barrier are currently being carried out worldwide [34–36].

This study is dealing with high entropy oxides (HEOs) [37], a new family of materials discovered in 2015 which has gained significant interest in recent years. The definition of a high entropy oxide relates to a multicationic oxide with a random and homogenous cation distribution that is entropy stabilized in a single sublattice. As key criteria for being classified as a HEO, four or five cations must be mixed, the equimolarity must be fulfilled to maximize the configurational entropy and the parent oxides must exhibit different

crystal structures with low solubility in each other. In such a manner, some of the mixed cations can adopt an original configuration that cannot be obtained with the existing simple oxides. This may lead to original redox properties because the electronic configuration differs. Moreover, given that the synthesis of HEO induces reversible high entropy variation, it could be interesting to integrate it in the reduction step of a thermochemical cycle. As such, the reduction temperature could be decreased by maintaining a sufficiently high reduction enthalpy for a good reactivity during the oxidation step. The configurational disorder of such compounds provides a new path to design and discover several new crystalline phases of materials. This novel type of compound presents a high versatility and the possibility to design materials with engineered properties for specific applications. Some new advances were discovered in the field of energy storage [38,39], electrochemistry [40], optics [41,42], thermal material [43] or catalytic activity [44]. The redox properties of several of these compounds were also investigated. Zhai et al. [45] first studied iron oxide-related HEOs during thermochemical cycles. Gao et al. [46,47] investigated the same compounds during microwave-assisted thermochemical cycles. Pianassola et al. [48] and Djenadic et al. [49] first synthesized a new HEO with a Ce_2O_3-related structure. These compounds could be interesting for thermochemical H_2/CO production as long as the authors demonstrated that Ce^{4+} cations are reducible in such structures. Sarkar et al. [50] as well as De Santiago et al. [51] studied the thermal cycling of several rare-earth high entropy perovskites. Furthermore, a promising high oxygen storage capacity of rocksalt HEO (Mg,Co,Ni,Cu,Zn)O was reported [52,53]. Therefore, a series of specific HEO materials formulations [45–54] were selected in this work as potentially attractive redox-active candidates for solar fuel production and their performances for two-step thermochemical redox cycles were evaluated, compared, and discussed.

2. Results and Discussion

The list of HEO materials investigated for the thermochemical redox cycle as well as the synthesis and characterization methods are reported in the Materials and Methods section (Section 3).

2.1. Iron Oxide-Based HEO (related to HEO 1 and HEO 2)

$Fe_{0.25}Mg_{0.25}Co_{0.25}Ni_{0.25}O_x$ (HEO 1) has been already characterized for thermochemical redox cycling by Zhai et al. [45] and Gao et al. [46]. In their investigations, they highlight a reversible phase swing during cycling between a rocksalt structure (reduced phase) and a spinel structure (oxidized phase). Both structures co-exist but the ratio between them changes during the thermal cycling.

The XRD patterns of the synthesized materials are presented in Figure 1. Both HEO 1 ($Fe_{0.25}Mg_{0.25}Co_{0.25}Ni_{0.25}O_x$) and HEO 2 ($(Fe_{0.25}Mg_{0.25}Co_{0.25}Ni_{0.25})Zr_{0.6}O_x$) materials calcined at 1000 °C in air possess a dual phase of spinel and rocksalt with a predominance of the spinel phase. HEO 2, which also contains Zr, displays a monoclinic ZrO_2 phase after annealing at 1000 °C. The heating at 1300 °C in air does not change the ratio between the two phases (spinel and rocksalt) but the width of the diffraction peaks decreases, thereby highlighting a crystallite growth. In HEO 2, the ZrO_2 phase changes from monoclinic to tetragonal. The XRD analysis after two complete thermochemical cycles is also shown in Figure 1. The rocksalt phase peak intensity increases for both HEO 1 and HEO 2. As the rocksalt phase corresponds to the reduced phase, this means that the CO_2-splitting step under these conditions does not allow the full reoxidation of these oxides.

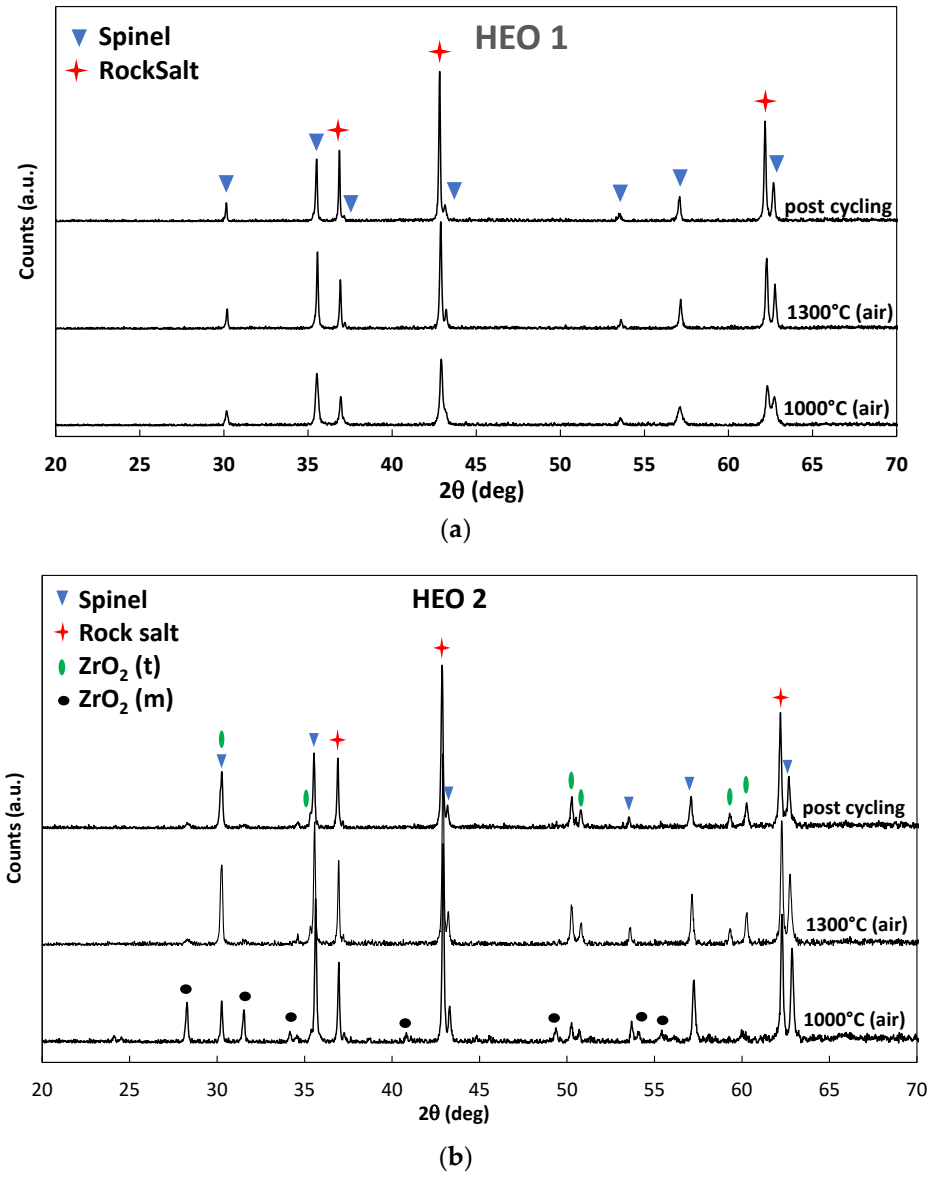

Figure 1. XRD patterns of (**a**) HEO 1 and (**b**) HEO 2 after calcination at 1000 °C, 1300 °C in air during 1 h and after two thermochemical cycles (post-cycling).

Figure 2 presents the temperature-programmed XRD analyses of HEO 1 during two consecutive cycles, thus under the real atmosphere conditions including reduction in inert gas followed by oxidation in CO_2. Diffractograms were recorded at different temperatures during the reduction step and the oxidation step. The temperature profile of the analysis is presented in Section 3. The predominant phase swing between spinel and rocksalt is observed (Figure 2b). During the reduction step, the relative intensity of the peak associated with the spinel structure ($2\theta = 35°$) decreases compared to the one of the rocksalt phase ($2\theta = 37°$) (Figure 2b). This phenomenon is reversible during the different steps of the thermochemical cycles. A peak shift toward low angles is also observed for all phases during heating. This peak shift is reversible during cooling.

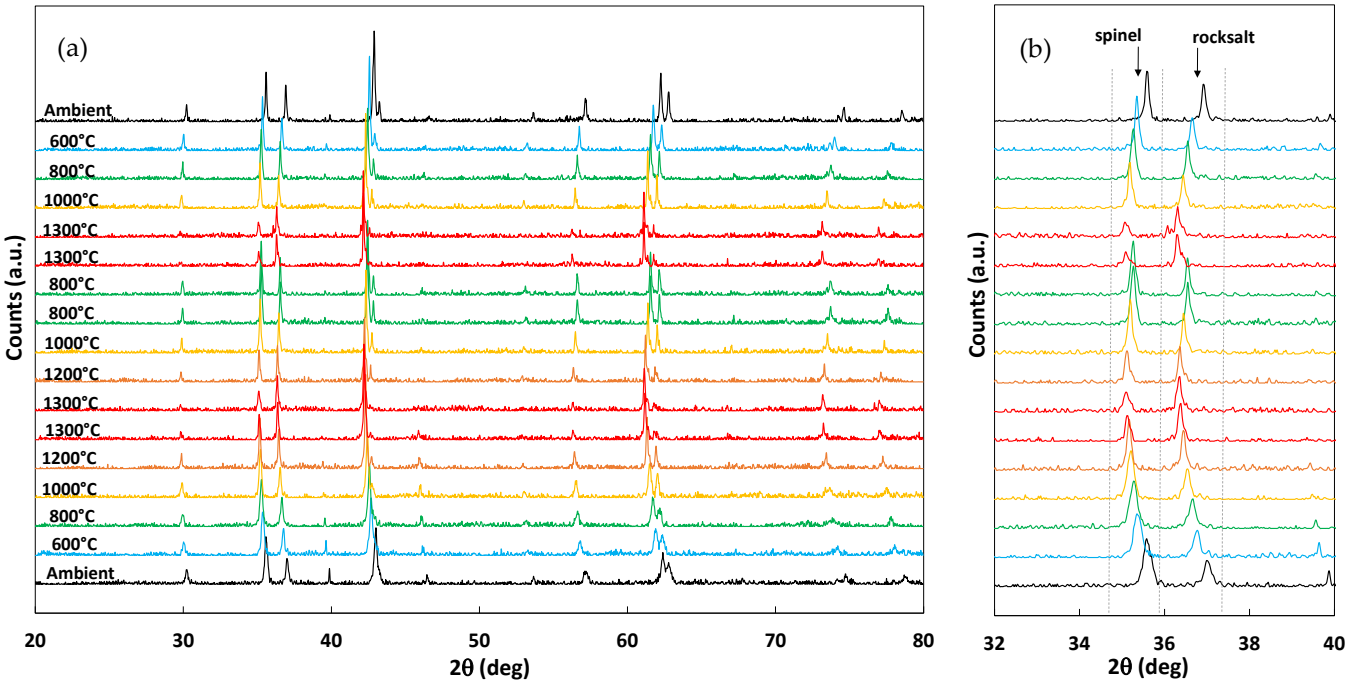

Figure 2. In situ XRD analysis of HEO 1 during two consecutive thermochemical cycles. (**a**) Full scale; and (**b**) Zoom from 2θ = 32°–40°.

The EDS analysis of HEO 2 is presented in Figure 3. The atomic distribution is not perfectly homogeneous, and it can be noticeably observed that iron atoms are not well distributed after annealing at 1300°C (Figure 3a) and after cycling (Figure 3c). Two different oxides are thus mixed in this material in good agreement with XRD analysis: an iron-rich phase (likely associated with the spinel phase) and a (Co,Ni,Mg)O oxide phase corresponding to the rocksalt phase. After thermochemical cycling, the cationic distribution is still heterogeneous. In contrast to previously published investigations on $Fe_{0.25}Mg_{0.25}Co_{0.25}Ni_{0.25}O_x$ [45–47], the entropy stabilization is not evidenced in the present study. Because a phase swing is observed like in the mentioned publications, the rocksalt phase and the spinel phase should result from the migration of iron during cycling.

(a)

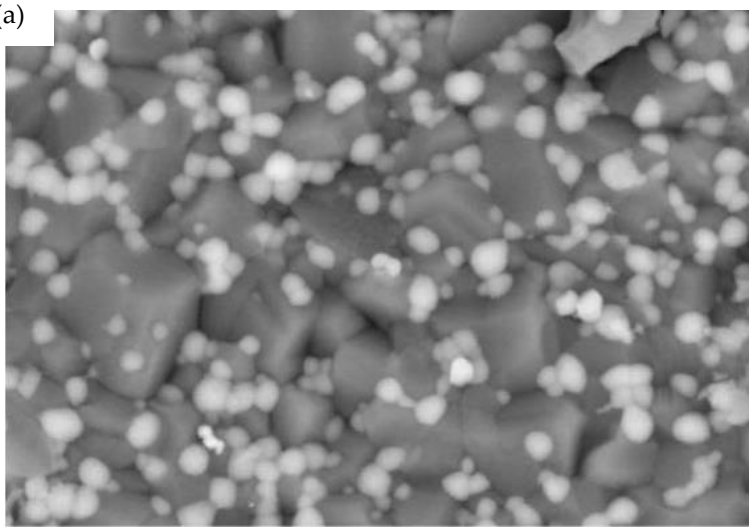

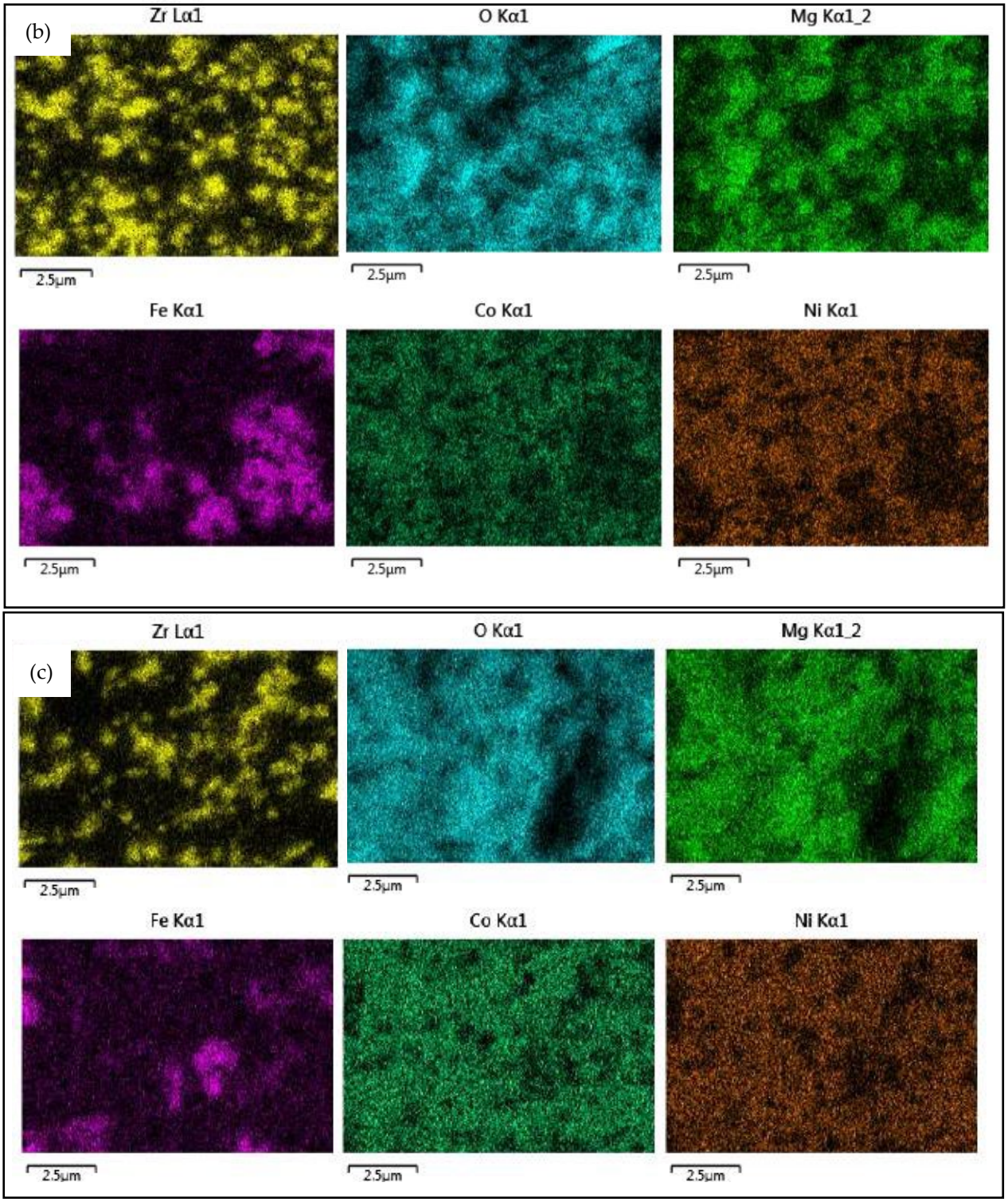

Figure 3. EDS analysis of HEO 2. (**a**) SEM analysis of HEO 2 after annealing at 1300 °C. (**b**) Elementary cartography after annealing in air at 1300°C, and (**c**) after thermochemical cycles.

Thermogravimetric analysis during two consecutive CO_2-splitting cycles is presented in Figure 4 and the quantitative production yields are reported in Table 1. The first reduction step at 1300 °C yields 185 and 174 µmol/g of oxygen for HEO 1 and HEO 2, respectively. During the first CO_2-splitting step, HEO 1 shows two distinct reaction stages, a first rapid mass increase followed by a slower mass increase. This must correspond to different oxidation mechanisms that lead to 154 µmol of CO produced per gram of oxide. HEO 2 produces 131 µmol of CO per gram with a steady mass increase. These amounts do not

correspond to a full re-oxidation of HEO 1 and HEO 2 but it can be observed that the mass uptakes are not fully completed when the CO_2 injection is stopped. Kinetics are indeed too slow to fully re-oxidize both materials. During the second cycle, the reduction step yields 111 and 78 µmol of O_2 per gram of oxide for HEO 1 and HEO 2, respectively. HEO 1 offers a higher reduction yield than HEO 2, however, during the re-oxidation step, HEO 2 produces slightly more CO, with 116 and 131 µmol of CO per gram for HEO 1 and HEO 2, respectively. The addition of zirconium in the material (HEO 2) enables stabilizing the CO production by avoiding a partial deactivation of the material during cycling compared to HEO 1. Comparing the CO production with state-of-the-art best-known materials (CeO_2 and $La_{0.5}Sr_{0.5}Mn_{0.9}Mg_{0.1}O_3$) under similar experimental conditions, both HEO 1 and HEO 2 do not overpass their performance in terms of kinetics or overall CO production (cf. Table 1).

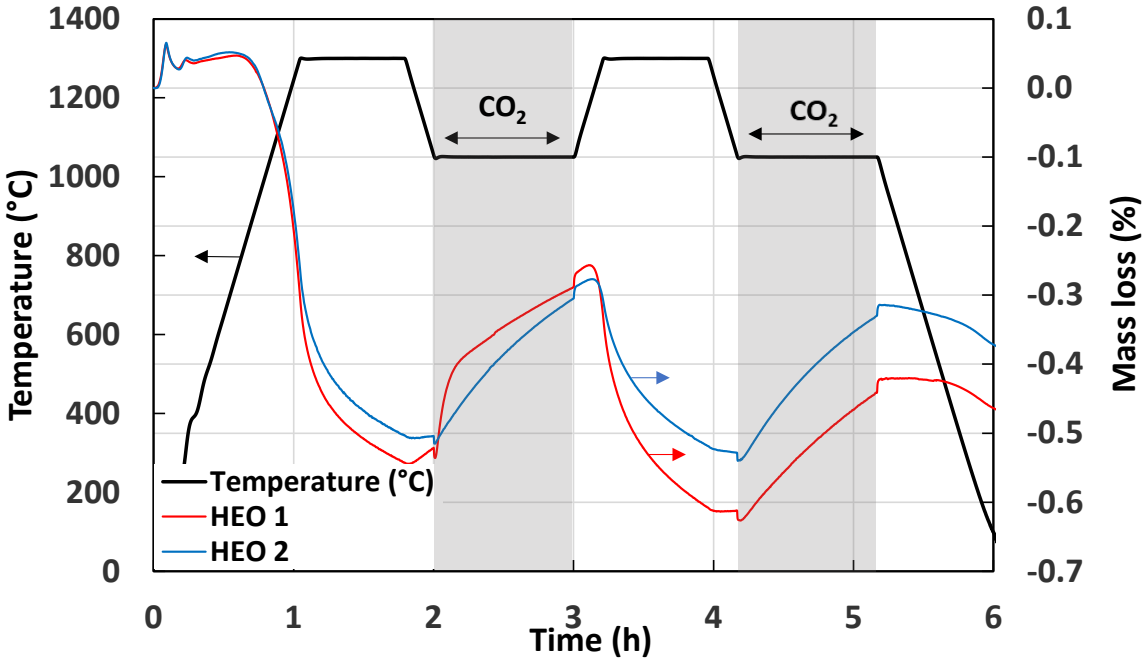

Figure 4. Thermogravimetric analysis of two consecutive CO_2-splitting cycles with HEO 1 and HEO 2.

Table 1. Summary of O_2 release and CO production yields during two consecutive thermochemical cycles with the considered high entropy oxides.

Name	First Reduction, O_2 Release (µmol/g)	First Oxidation, CO Production (µmol/g)	Second Reduction, O_2 Release (µmol/g)	Second Oxidation, CO Production (µmol/g)
HEO 1	185	154	111	116
HEO 2	174	131	78	131
HEO 3	259	23	233 (*1000 °C*)	0 (*600 °C*)
HEO 4	143	99	79	90
HEO 5	128	81	62	79
HEO 6	276	87	63	83

HEO 7	407	44	153	20
CeO_2	50	102	53	105
LSMMg	254	246	203	249

Compared to the values reported in the literature, the performances measured for HEO 1 and HEO 2 are far below those obtained with $Fe_{0.25}Mg_{0.25}Co_{0.25}Ni_{0.25}O_x$ [45] (450 µmol of H_2 per gram). However, the experimental conditions strongly differ and are much more favorable in [39], with a H_2:H_2O ratio of 10^{-3}, a re-oxidation temperature of 800 °C and 5 h for reduction and oxidation steps. Even higher performances were obtained from microwave-assisted thermochemical cycles (2830 µmol and 4840 µmol of H_2 per gram with HEO 1 and HEO 2, respectively) [46,47].

2.2. Ceria-Based HEO (Related to HEO 3)

The HEO 3 formula is $(Ce_{0.2}La_{0.2}Pr_{0.2}Sm_{0.2}Y_{0.2})_2O_3$, and this compound has the specificity to integrate Ce^{4+} cations in a typical Ce^{3+} oxide structure, which is a C-type cubic structure [48,49]. It has been reported that Ce^{4+} is reducible in this structure; thus, this study deals with the possibility of reoxidizing it by splitting CO_2 during redox cycles, which has never been investigated before. The XRD pattern of HEO 3 is presented in Figure 5. A single structure corresponding to the C-type cubic structure is observed after calcination at 1000 °C. This result differs from those obtained for solid-state synthesised materials as the single structure is only observed after annealing at 1500 °C in this case [48].

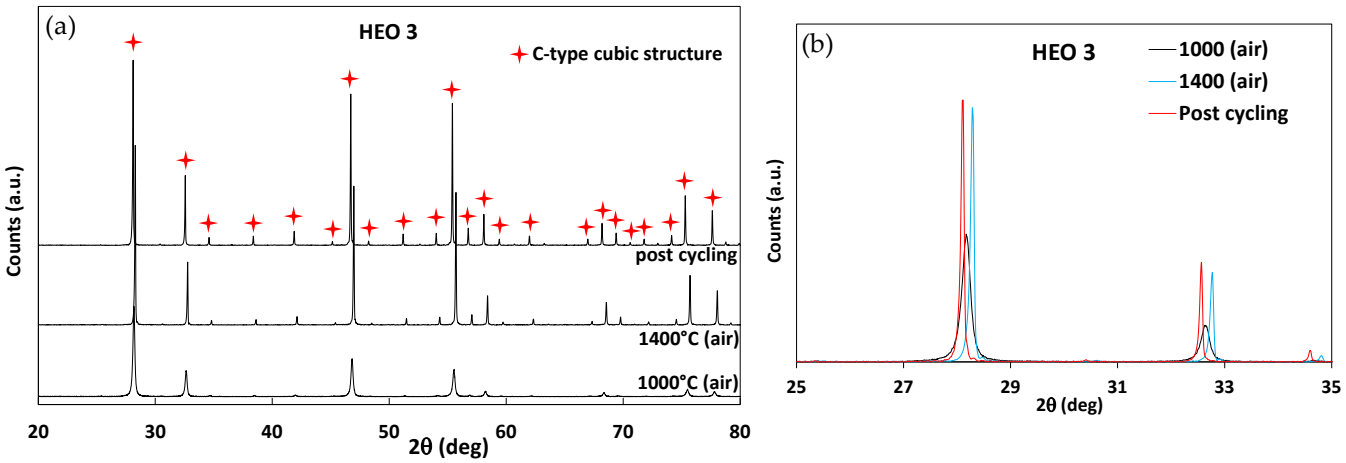

Figure 5. XRD analysis of $(Ce_{0.2}La_{0.2}Pr_{0.2}Sm_{0.2}Y_{0.2})_2O_3$ after different heat treatments (annealing in air during 1 h or thermal cycling): (**a**) complete diffractograms; and (**b**) zoom.

The lattice parameter (a) was calculated using the Bragg Formula (3).

$$2.d_{hkl}.sin\theta = n.\lambda \quad (3)$$

Given that the lattice is cubic, the relation between the inter-reticular distance and the lattice parameter is given by (4).

$$a = d_{hkl}.\sqrt{h^2 + k^2 + l^2} \quad (4)$$

By combining these two equations,

$$a = \frac{\lambda}{2.\sin\theta}.\sqrt{h^2 + k^2 + l^2} \quad (5)$$

Values of the lattice parameter are reported in Table 2. The calculated values (a = 10.966 Å after annealing at 1000 °C) fit those found in the literature (a = 10.956 Å [49]). After a heat treatment at 1400 °C, the lattice parameter decreases.

Table 2. Lattice parameter of HEO 3.

Heat Treatment	Lattice Parameter, a (Å)
1000 °C-1 h-in air	10.966 (±0.006)
1400 °C-1 h-in air	10.929 (±0.006)
Post cycling	10.990 (±0.006)

EDS analysis mappings are shown in Figure 6. The atomic cartography confirms the randomized distribution of cations. The atomic ratio of the different elements is in good agreement with the desired composition (Table 3): the corresponding composition is $(Ce_{0.20}La_{0.21}Pr_{0.19}Sm_{0.23}Y_{0.19})_2O_{2.95}$ after annealing at 1400°C and $(Ce_{0.19}La_{0.19}Pr_{0.18}Sm_{0.23}Y_{0.20})_2O_{2.99}$ after cycling.

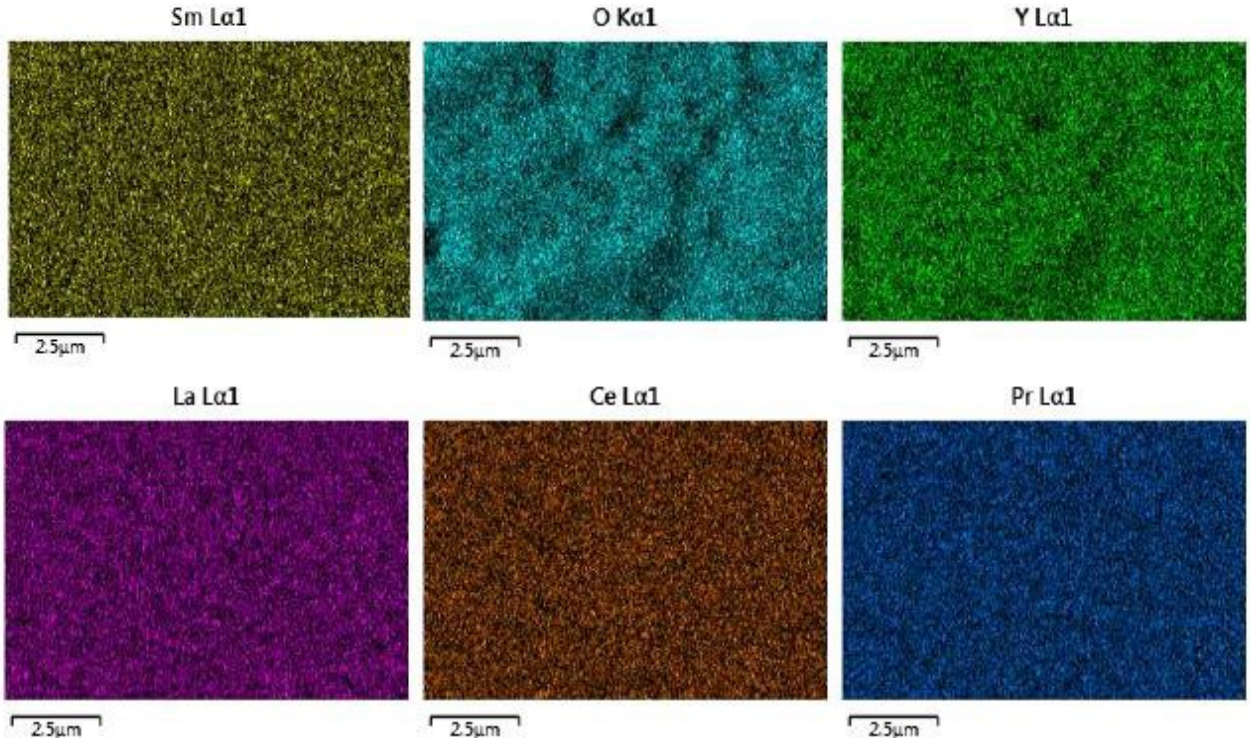

(**a**)

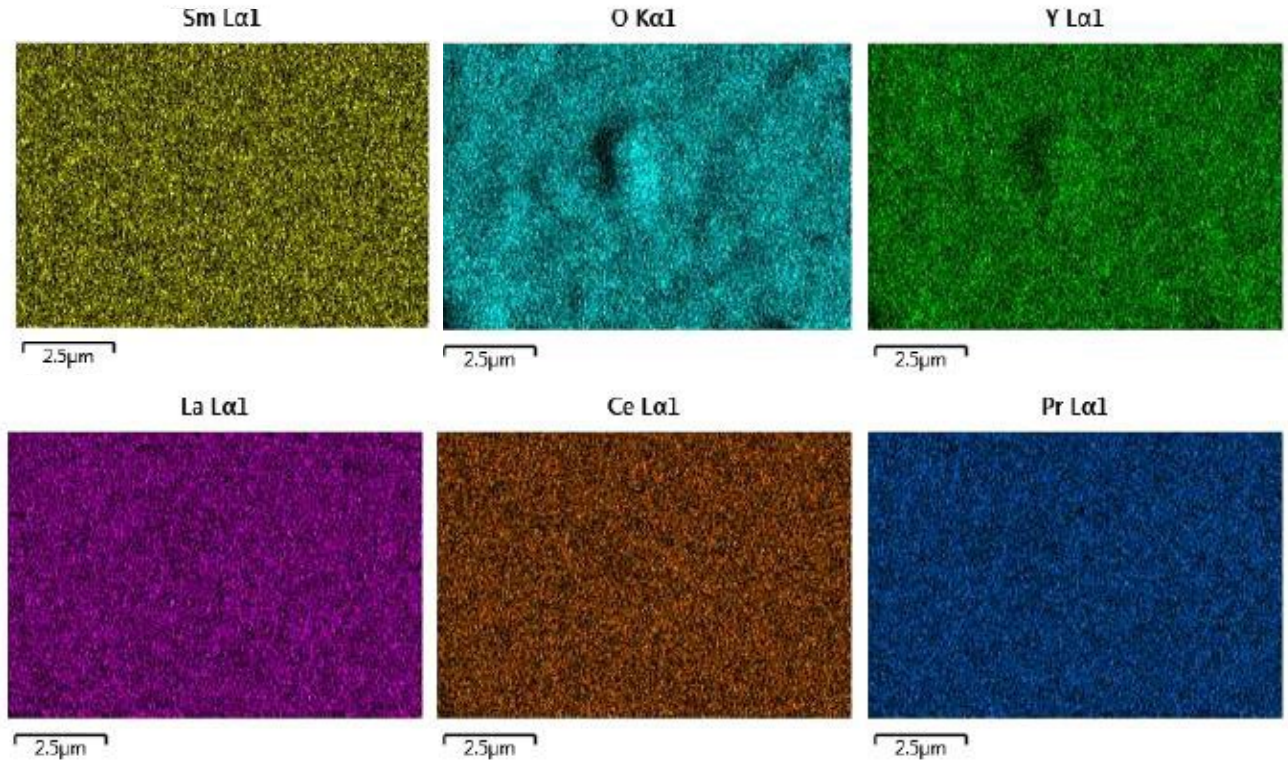

(**b**)

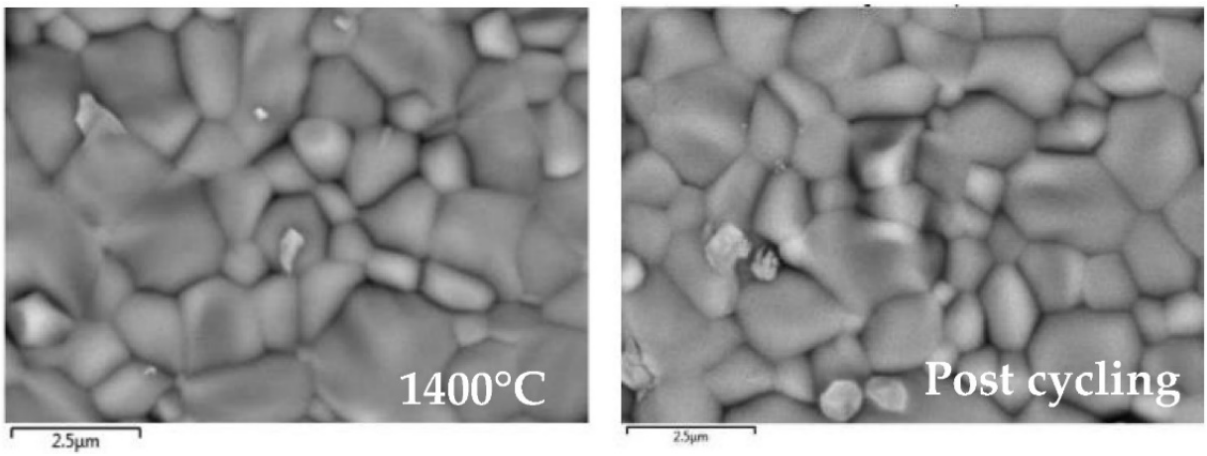

(**c**)

Figure 6. EDS analysis of HEO 3: (**a**) elementary cartography after annealing at 1400 °C; and (**b**) after cycling. (**c**) SEM analysis of HEO 3 before and after cycling.

Table 3. Elemental composition of HEO 3 measured by EDS.

Elements	% (Atomic)	
	After Annealing at 1400 °C	After Cycling
O	58.98	59.85
Y	7.89	8.09
La	8.34	7.89
Ce	7.95	7.56
Pr	7.71	7.33
Sm	9.13	9.28
Total %	100	100

The thermogravimetric analyses of CO_2-splitting cycles are presented in Figure 7. In Figure 7a, HEO 3 was heated until 1400 °C and CO_2 was injected at 1050 °C. During the reduction step, the mass loss reaches 0.84%, which corresponds to an oxygen amount of 259 µmol/g. However, the re-oxidation yield is very low with only 23 µmol of CO produced at 1050 °C. Because the reduction in HEO 3 starts at a low temperature (500 °C), during the re-oxidation step at 1050 °C, competition between the reduction and oxidation reactions may occur, explaining the low amount of CO produced. Another thermochemical cycle was performed at a lower temperature (1000 °C for reduction and 600 °C for re-oxidation) to observe whether the CO production could be improved (Figure 7b). The reduction yield at 1000 °C is still high with 233 µmol of O_2 per gram, however, the reduced material does not react with CO_2 at 600 °C. Although HEO 3 appears to be easily reducible, its reduced counterpart cannot be re-oxidized with CO_2 in these conditions. Further investigations such as XPS analysis could help understand why the reduced material is not reactive with CO_2 even though Ce^{3+} is present in the reduced phase. Charvin et al. [55] studied mixed cerium oxides with a pyrochlore structure in which Ce^{3+} was also not directly reactive with water and required an additional activation step (3-step cycle) to re-oxidize Ce^{3+}, showing that Ce^{3+} can be less reactive in a different structure, in comparison with non-stoichiometric ceria. The calculated lattice parameter is larger after cycling (Table 3), which confirms that the reduced species still remain after cycling because reduced cations have a larger ionic radius than oxidized ones. HEO 3 keeps its chemical composition (Table 3) and structure (Figure 5) after cycling without any phase modification.

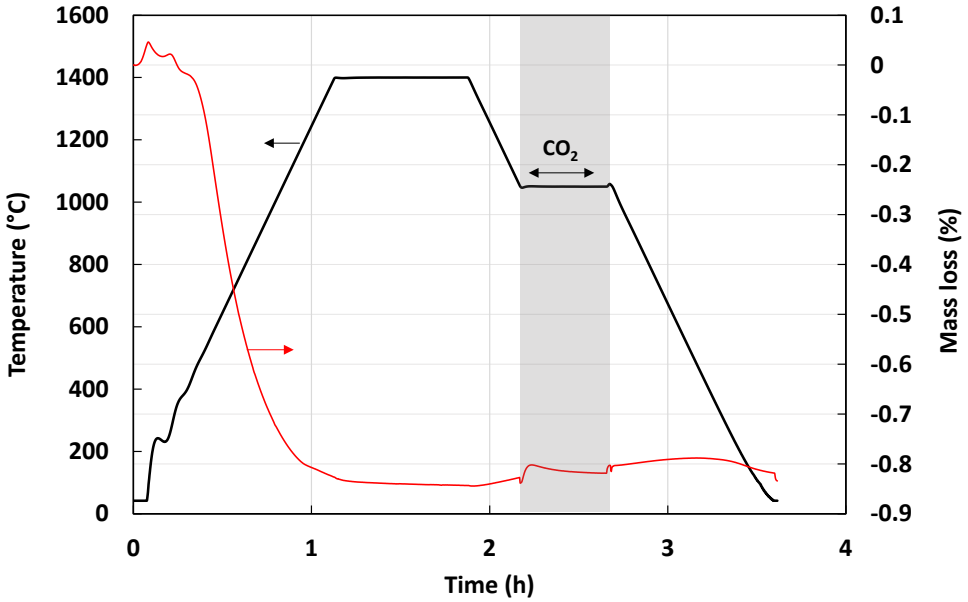

(a)

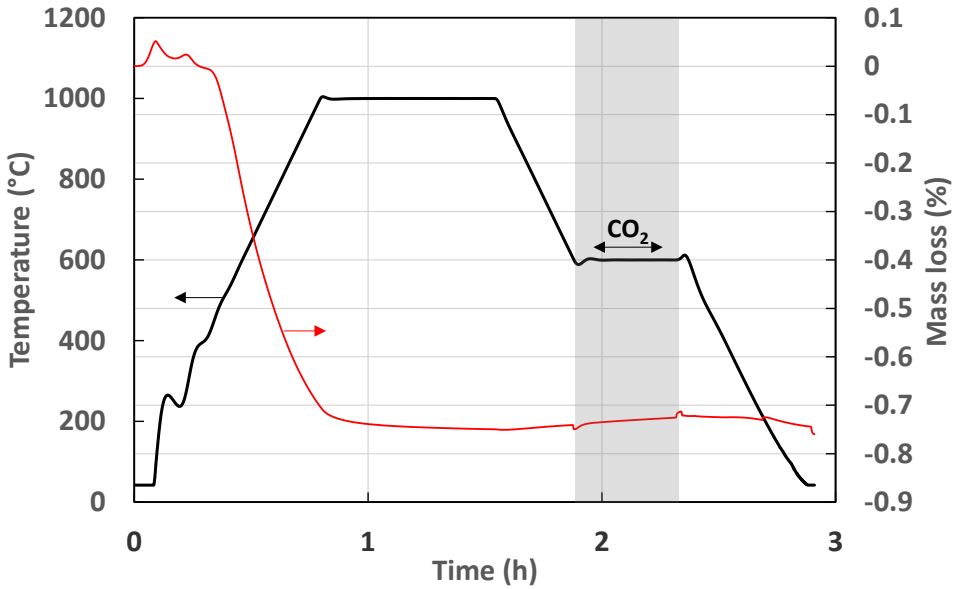

Figure 7. Thermogravimetric analysis of CO_2-splitting cycles with HEO 3. (**a**) Reduction step at 1400 °C and oxidation step at 1050 °C; and (**b**) reduction step at 1000 °C and oxidation step at 600 °C.

Figure 8 presents the high-temperature XRD diffractograms recorded during two consecutive cycles. The temperature profile of the in-situ analysis is presented in the Materials and Methods section (Section 3). This analysis confirms that no phase change happens during cycling. A peak shift to lower angles is observed when the material is heated up to 1400°C but it does not correspond to an effect of material reduction because it is reversible during cooling whereas the TGA analysis highlights that no re-oxidation occurs.

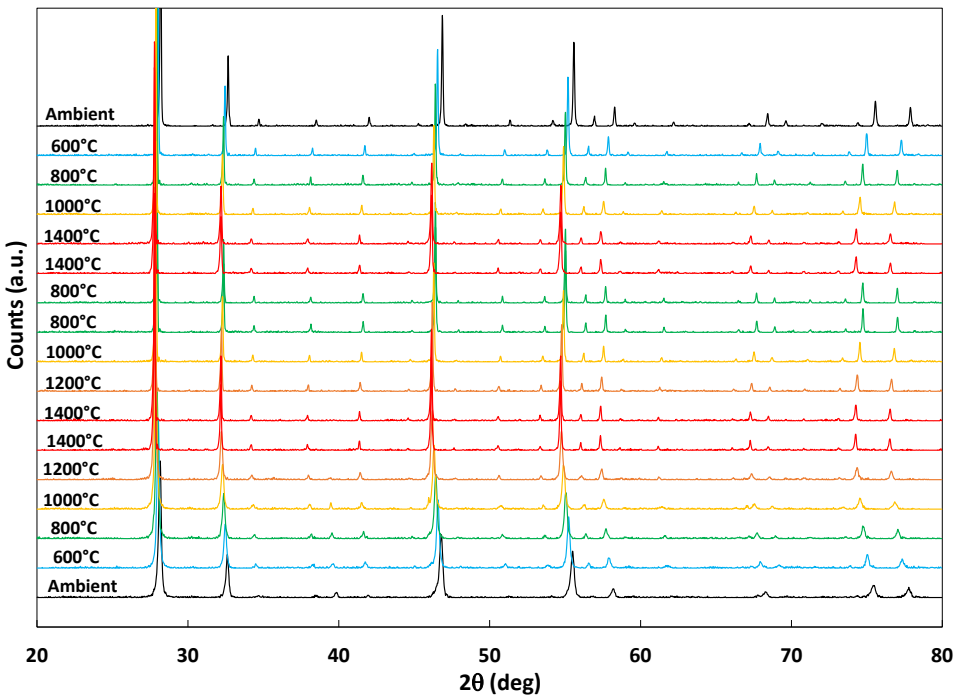

Figure 8. In situ XRD analysis of HEO 3 during two consecutive thermochemical cycles.

2.3. Perovskites-Based HEO (Related to HEO 4, HEO 5 and HEO 6)

HEO 4, HEO 5 and HEO 6 are perovskite-structured materials related to high entropy oxides. The desired chemical compositions are, respectively, $(Gd_{0.2}La_{0.2}Nd_{0.2}Sm_{0.2}Y_{0.2})(Co_{0.2}Cr_{0.2}Fe_{0.2}Mn_{0.2}Ni_{0.2})O_3$, $(La_{0.5}Sr_{0.5})(Mn_{0.2}Ce_{0.2}Ni_{0.2}Mg_{0.2}Cr_{0.2})O_3$ and $(La_{0.8}Sr_{0.2})(Mn_{0.2}Fe_{0.2}Co_{0.4}Al_{0.2})O_{3-\delta}$. XRD analyses of the compounds are shown in Figure 9 after different heat treatments and after thermochemical cycling.

HEO 4 presents a single-phase structure after annealing at 1000 °C, corresponding to an orthorhombic perovskite related to $SmCrO_3$. The entropy-stabilized phase has been obtained at 1000 °C. The atomic composition derived from EDS corresponds to $(Gd_{0.20}La_{0.22}Nd_{0.22}Sm_{0.33}Y_{0.20})(Co_{0.18}Cr_{0.20}Fe_{0.21}Mn_{0.20}Ni_{0.21})O_{2.73}$, in good agreement with the desired composition. The EDS analysis reveals a homogeneous cation distribution at 1400 °C, except for an isolated yttrium-rich particle (Figure 10a) that was confirmed by XRD at 1400 °C (Figure 9). Indeed, at 1400 °C, a secondary phase appears on the XRD pattern and, after cycling, several additional phases are observed with an increased peak intensity. EDS after cycling shows a heterogeneous composition, in which three phases are observed. The SEM micrographs (Figure 10b) reveal dark particles that are composed of Co, Ni and O (EDS), bright particles of yttrium oxide and grey particles corresponding to the desired perovskite phase. The XRD analysis reveals that the new phases observed after cycling correspond to the NiO-type phase (NiCoO) and Y_2O_3-type phase $(Y,Sm,Gd)_2O_3$.

HEO 5 should also have a single crystallographic structure corresponding to a cubic perovskite. Unfortunately, a multi-phase composition is revealed by XRD analysis whatever the annealing temperature. The mix is composed of phases related to CeO_2, MgO, Sr_2MnO_4 and the cubic perovskite $LaMnO_3$. Even after annealing at 1400 °C for 3 h, the single phase is not formed. The non-homogeneity of the material was confirmed by EDS, with the detection of four different phases/areas including CeO_2, a (Mg,Ni) oxide, a Sr-rich phase associated with Mn and O, and a (La,Mn)O phase (Figure 10).

The XRD analysis of HEO 6 reveals a single structure after annealing at 1000 °C in air. The crystallographic structure is related to the $LaMnO_3$ perovskite. After annealing at 1300 °C, diffraction peaks are split, which means that a second perovskite phase with a different chemical composition appears after annealing.

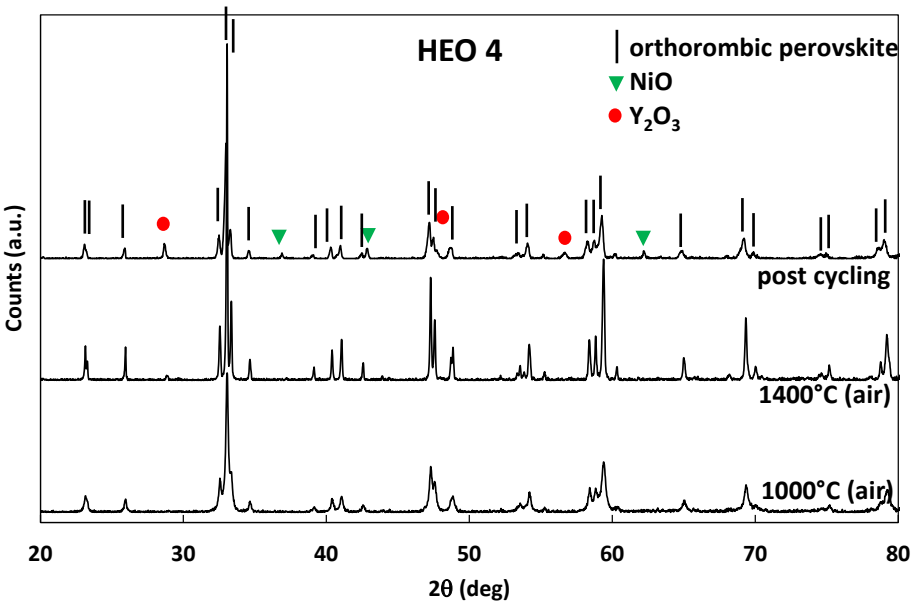

(**a**)

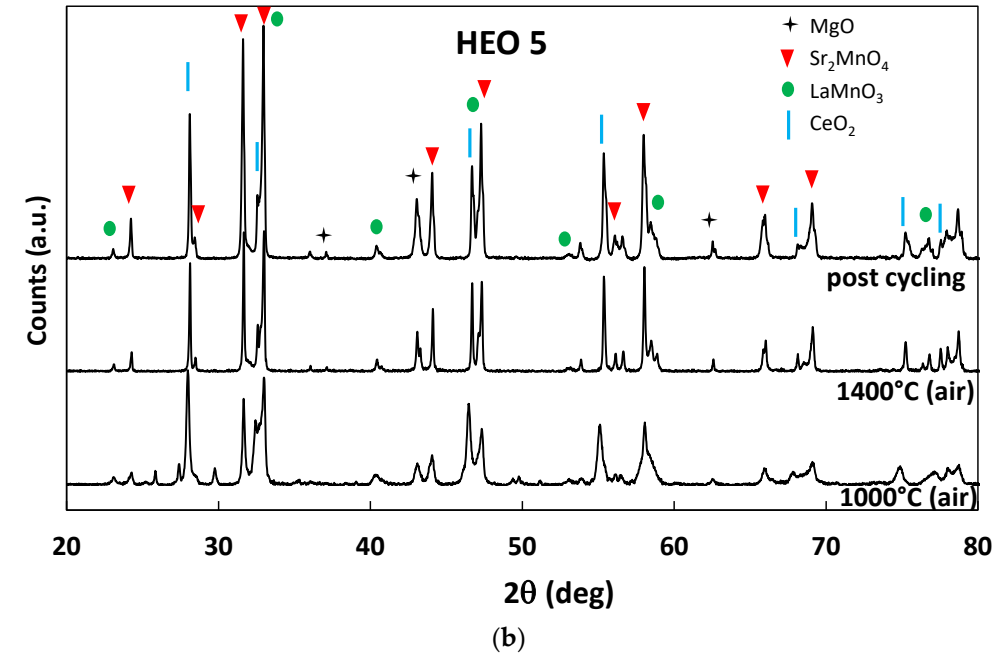

(**b**)

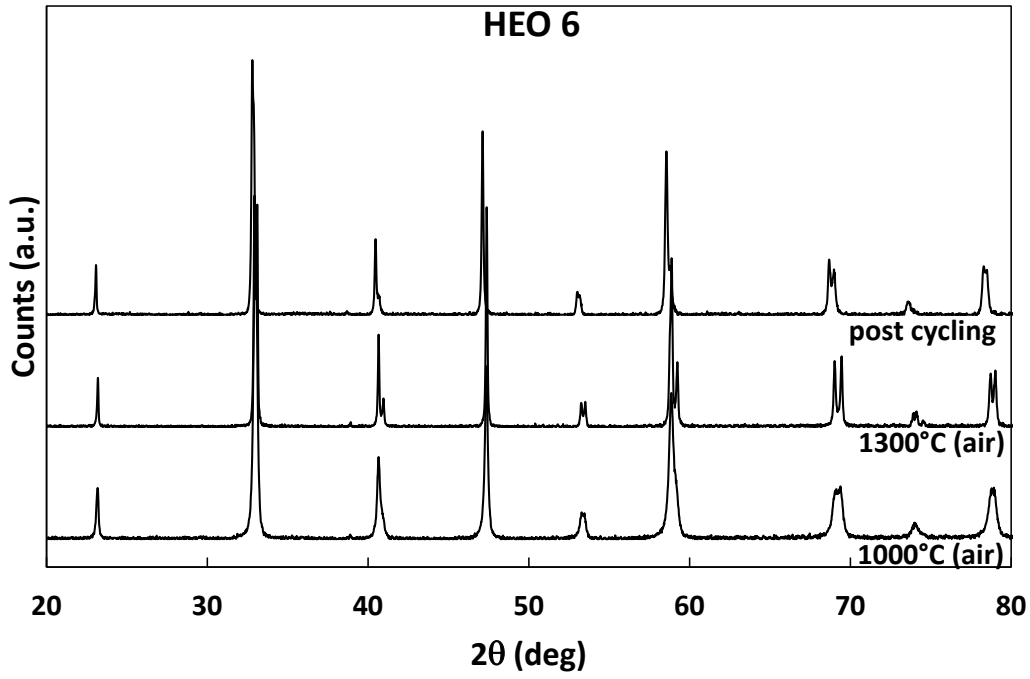

(**c**)

Figure 9. XRD analysis of (**a**) HEO 4, (**b**) HEO 5 and (**c**) HEO 6 after different heat treatments in air (1 h) and after thermochemical cycling.

The thermograms of two consecutive CO_2-splitting cycles with HEO 4, HEO 5 and HEO 6 are presented in Figure 11. The TGA of $La_{0.5}Sr_{0.5}Mn_{0.9}Mg_{0.1}O_3$ (LSMMg) is added to compare with the best-in-the-class perovskite. The performances of HEO 4, HEO 5, and HEO 6 do not overpass LSMMg with production yields of 143, 128 and 276 µmol/g of O_2 during the first reduction step at 1400 °C, and 79, 62 and 63 µmol/g during the second reduction step, respectively (Table 1). The CO production of HEO 4, HEO 5 and HEO 6 reaches 99 µmol/g, 81 µmol/g and 87 µmol/g during the first cycle, and 90 µmol/g, 79 µmol/g and 83 µmol/g during the second cycle, respectively. These CO amounts are stable during cycling but still much lower than those measured with LSMMg. Such low

performances are explained by the multi-phase that appears during cycling in HEO 4 and HEO 5. Indeed, the NiO-type and Y_2O_3-type phases are not reactive during thermochemical CO_2-splitting cycles. Only the orthorhombic phase might react with CO_2 in HEO 4, and only CeO_2 and the cubic perovskite might react in HEO 5. HEO 6 shows a high reduction yield during the first heating at 1400 °C such as LSMMg, but the re-oxidation steps are associated with slow kinetics that lead to a poor CO production yield.

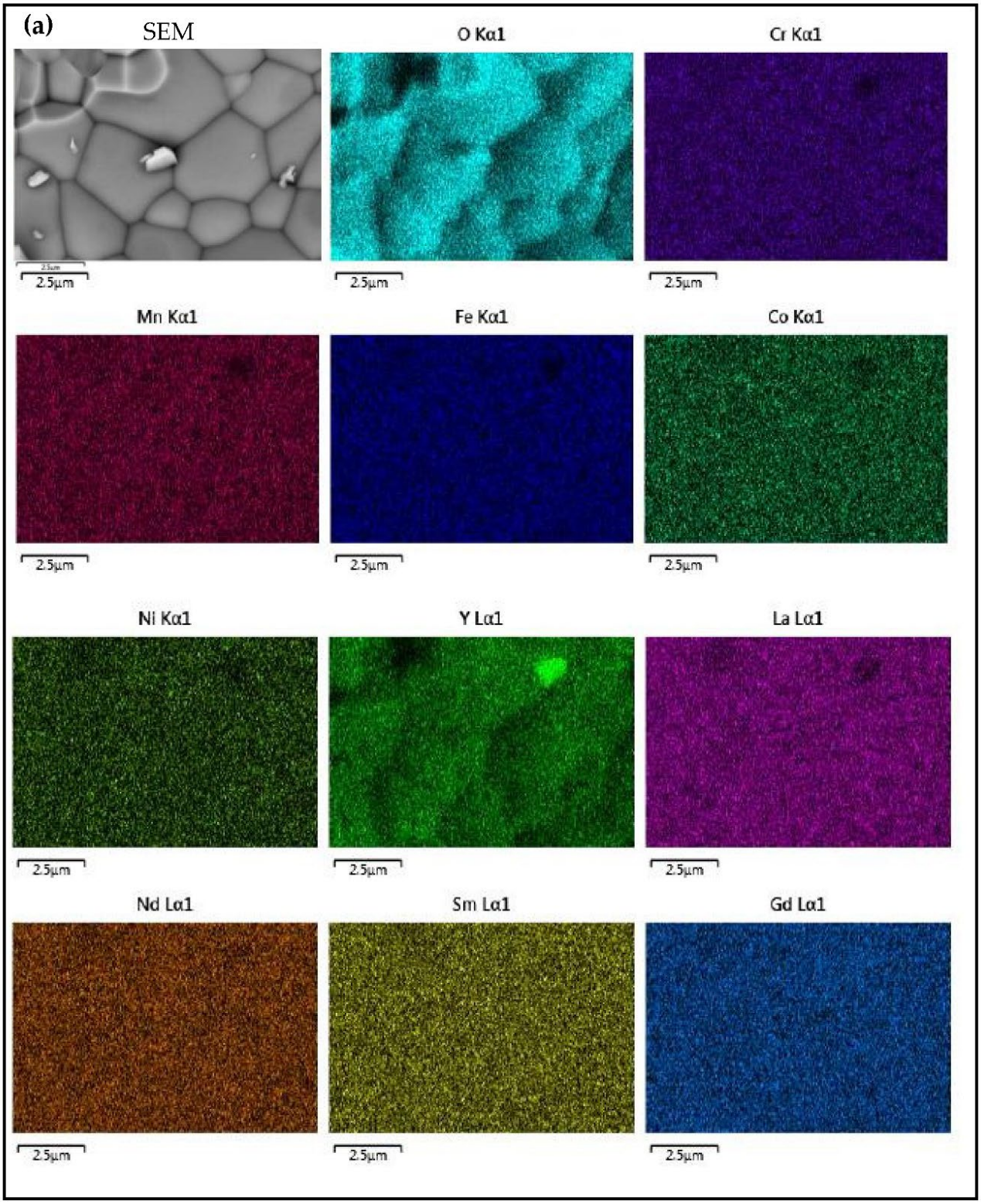

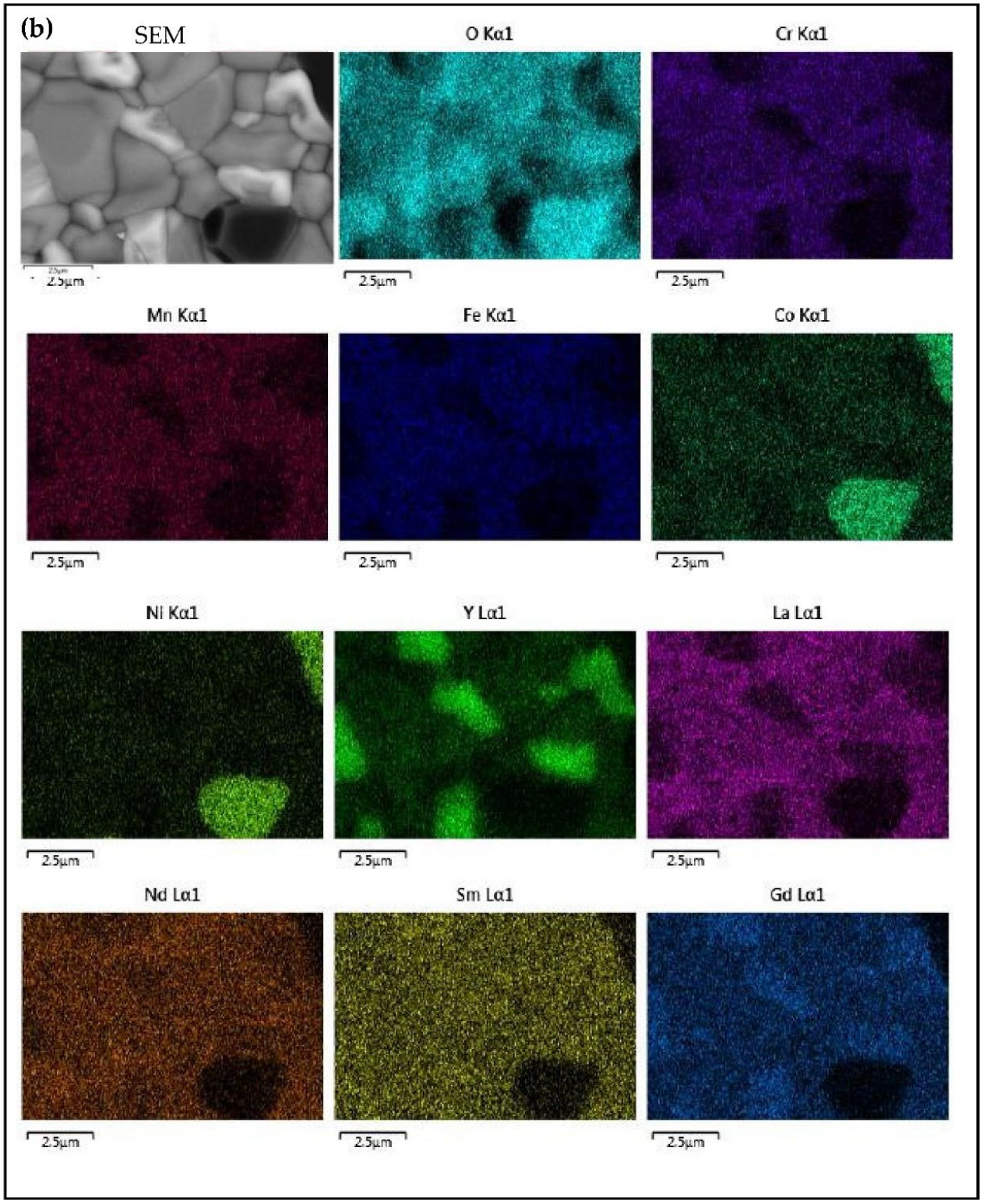
(b)
SEM
O Kα1
Cr Kα1
Mn Kα1
Fe Kα1
Co Kα1
Ni Kα1
Y Lα1
La Lα1
Nd Lα1
Sm Lα1
Gd Lα1
2.5μm

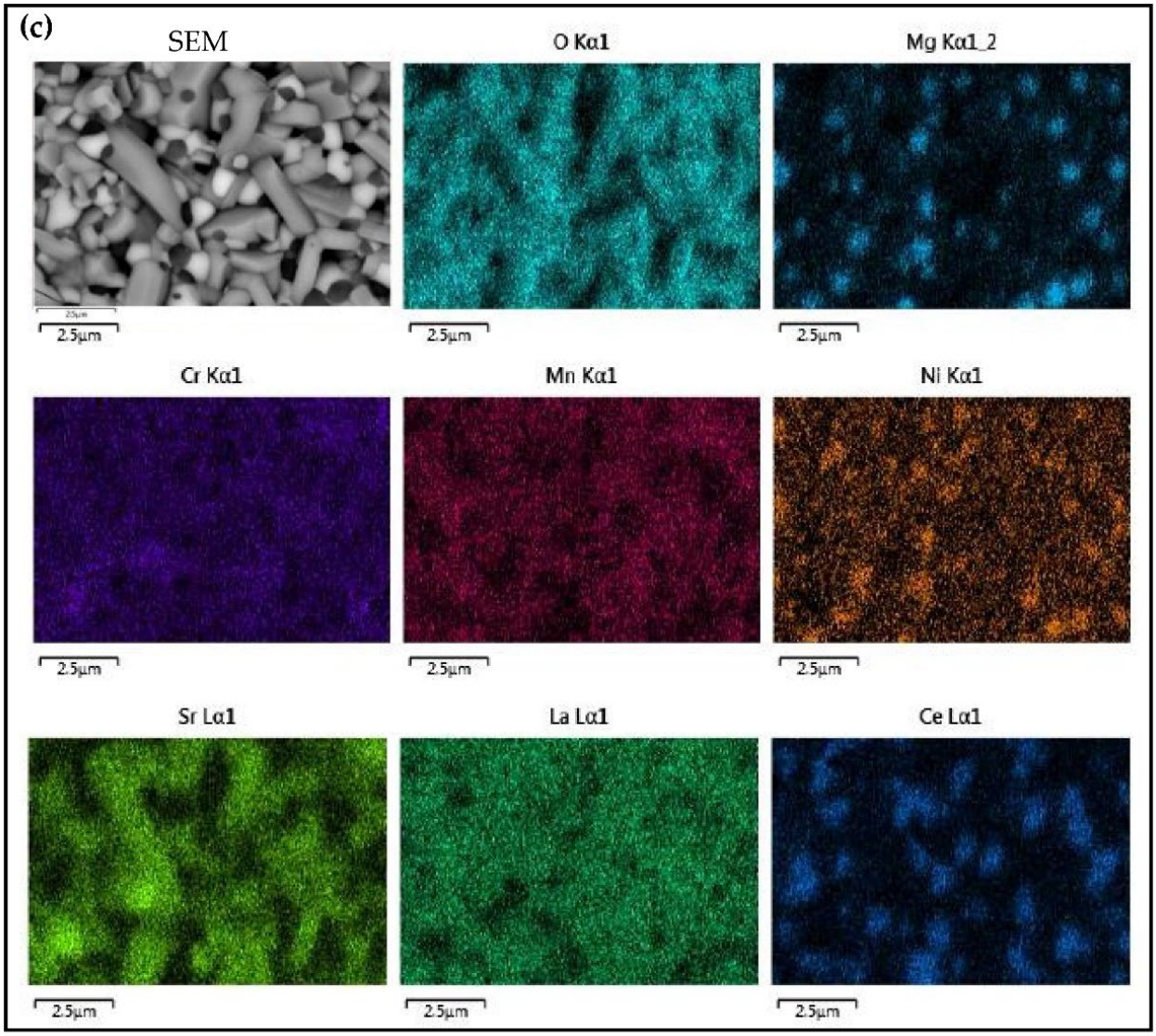

Figure 10. EDS analysis of HEO 4 and HEO 5. (**a**) elementary cartography of HEO 4 after annealing at 1400°C and (**b**) after cycling. (**c**) Elementary cartography of HEO 5 after annealing at 1400 °C.

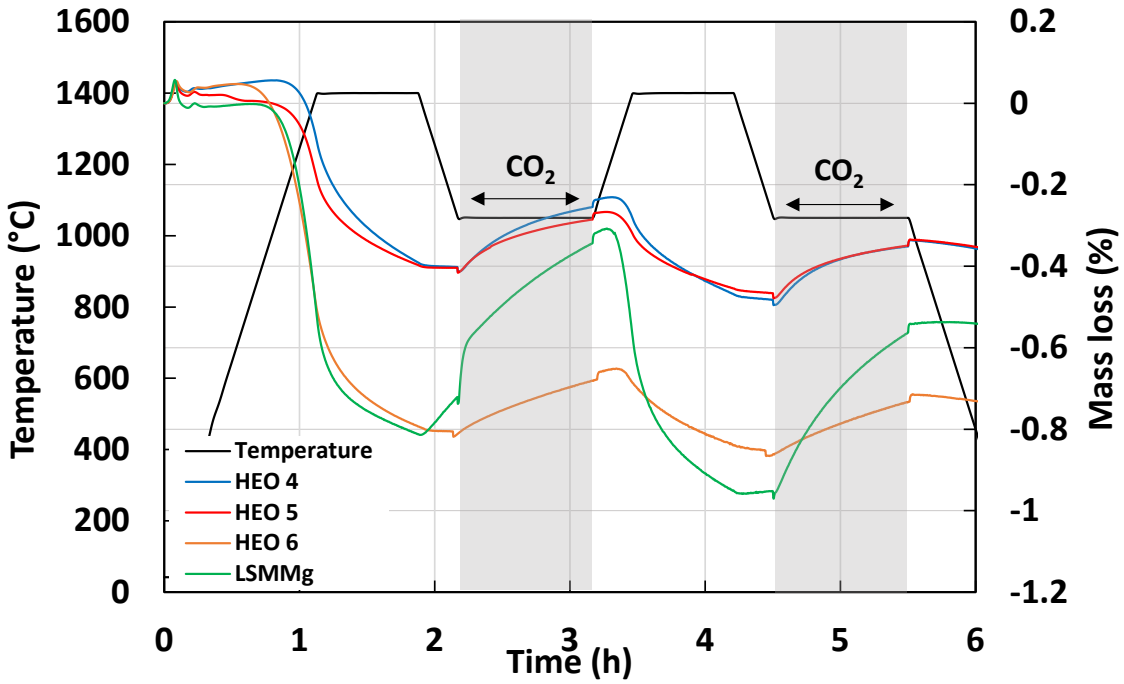

Figure 11. Thermogravimetric analysis of two consecutive CO_2-splitting cycles with HEO 4, HEO 5 and HEO 6 in comparison with $(La_{0.5}Sr_{0.5})Mn_{0.9}Mg_{0.1}O_3$.

2.4. Ferrite-Based HEO (Related to HEO 7)

The chemical composition of HEO 7 is $(Mg_{0.2}Co_{0.2}Ni_{0.2}Cu_{0.2}Zn_{0.2})Fe_2O_4$. The crystallographic structure is related to classical ferrites as shown in Figure 12. The calculated lattice parameter is a = 8.386(6) Å at 1000°C and a = 8.388(6) Å at 1300 °C.

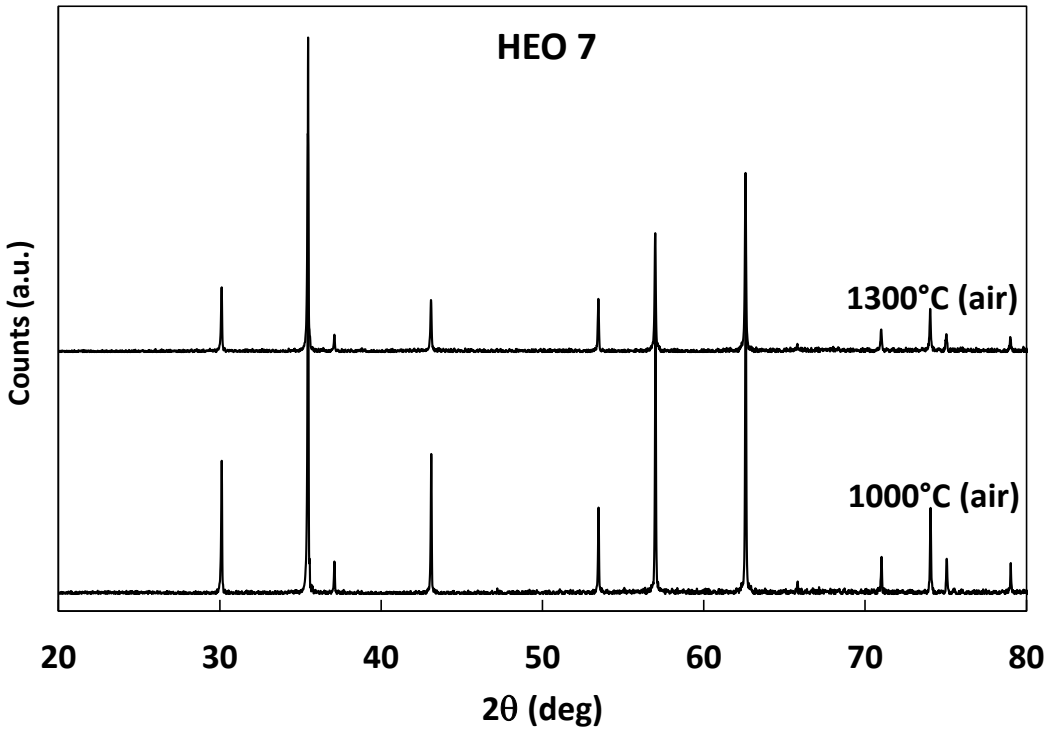

Figure 12. XRD analysis of HEO 7 after annealing at 1000 °C and 1300 °C in air for 1 h.

The thermogravimetric analysis of two consecutive CO_2-splitting cycles with HEO 7 is presented in Figure 13. During the first reduction at 1300 °C, a strong mass decrease is observed corresponding to an O_2 release of 407 µmol/g (Table 1). Nevertheless, the reduced HEO 7 does not significantly react with CO_2 during the oxidation step with only 44 µmol/g of CO. During the second cycle, the material still continues to release oxygen at 1300 °C (153 µmol/g) but a very small mass increase occurs during the oxidation step (20 µmol/g of CO).

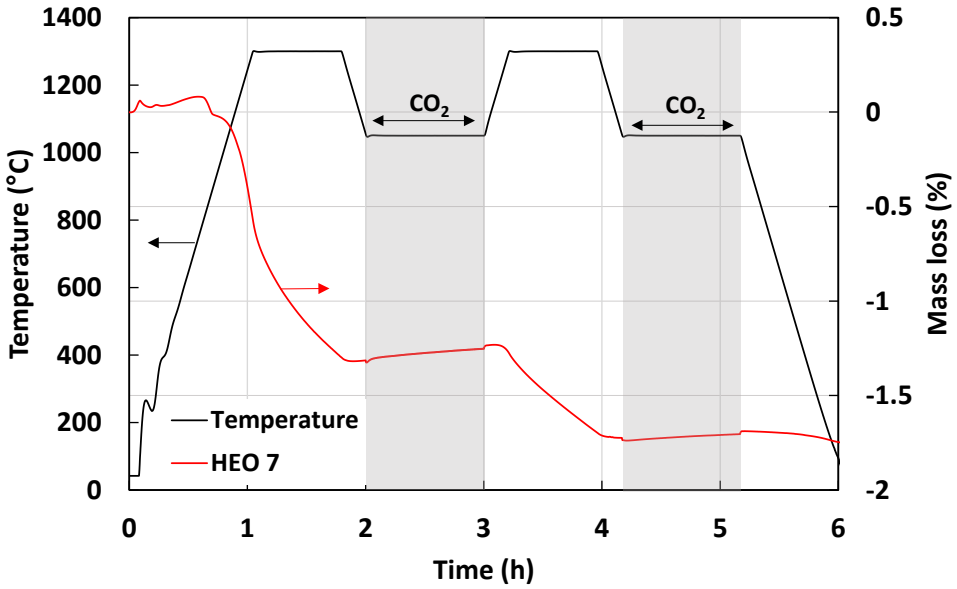

Figure 13. Thermogravimetric analysis of two consecutive CO_2-splitting cycles with HEO 7.

3. Materials and Methods

3.1. Materials Synthesis

Table 4 lists the different materials investigated in this study. Compositions of the high entropy oxides were either chosen from literature data related to an investigation of their reducibility, or because they incorporate reducible Ce^{4+} or Fe^{3+} cations in an original configuration.

Table 4. List of HEO materials investigated for thermochemical redox cycles.

Name	Compositions	Structure	References
HEO 1	$Fe_{0.25}Mg_{0.25}Co_{0.25}Ni_{0.25}O_x$	Rocksalt/spinel	[45,46]
HEO 2	$(Fe_{0.25}Mg_{0.25}Co_{0.25}Ni_{0.25})Zr_{0.6}O_x$	Rocksalt/spinel	[47]
HEO 3	$(Ce_{0.2}La_{0.2}Pr_{0.2}Sm_{0.2}Y_{0.2})_2O_3$	Cubic type C	[48,49]
HEO 4	$(Gd_{0.2}La_{0.2}Nd_{0.2}Sm_{0.2}Y_{0.2})(Co_{0.2}Cr_{0.2}Fe_{0.2}Mn_{0.2}Ni_{0.2})O_3$	Perovskite	[50]
HEO 5	$(La_{0.5}Sr_{0.5})(Mn_{0.2}Ce_{0.2}Ni_{0.2}Mg_{0.2}Cr_{0.2})O_3$	Perovskite	
HEO 6	$(La_{0.8}Sr_{0.2})(Mn_{0.2}Fe_{0.2}Co_{0.4}Al_{0.2})O_{3-d}$	Perovskite	[51]
HEO 7	$(Mg_{0.2}Co_{0.2}Ni_{0.2}Cu_{0.2}Zn_{0.2})Fe_2O_4$	Spinel	[54]

These materials (#HEO 1–7) were synthesized by using the modified Pechini method described elsewhere [56]. Briefly, metallic nitrate precursors were dissolved in distilled water under stirring during 10 min. Citric acid was then added to the solution under stirring with a molar concentration twice that of the cations concentration ($n_{CA} = 2 \times n_{cations}$). Ethylene glycol was then poured into the solution with a molar concentration 4-fold that of the cations concentration ($n_{EG} = 4 \times n_{cations}$). The solution was stirred and heated at 90 °C until gelation (brownish color). The gel was then heated in a furnace at 250 °C for two

hours; the resulting powder was crushed in an agate mortar and calcined in air at 1000 °C during 1 h. To prevent any sintering effect during the thermal analysis, the oxides were then calcined in air during one hour at either 1300 °C or 1400 °C, corresponding to the maximum temperature of the TGA analysis.

3.2. Materials Characterization

The obtained powders were first characterized by X-ray diffraction (XRD) using a Panalytical X'PERT PRO diffractometer with the Cu Kα radiation (αCu = 0.15406 nm, angular range = 20–80°, 2θ, tube current 20 mA, potential 40 kV). The diffraction patterns were compared with those from the literature and lattice parameters were calculated.

High-temperature X-ray diffractometer (HT XRD- Empyrean Panalytical with Anton-Paar HTK1 chamber) equipped with Cu Kα radiation was used for the in-situ investigation of phase reactivity/transitions during redox cycling (tube current 20 mA, potential 45 kV, angular range = 20–80°, 2θ, angle variation 0.02626 °/s). The temperature profile of the in-situ analysis is presented in Figure 14. The powder was heated up to 1300 or 1400 °C under nitrogen flow for the reduction step and cooled down to 800 °C for the oxidation step with CO_2 injection. Two consecutive cycles were performed for a total of 17 diffractograms.

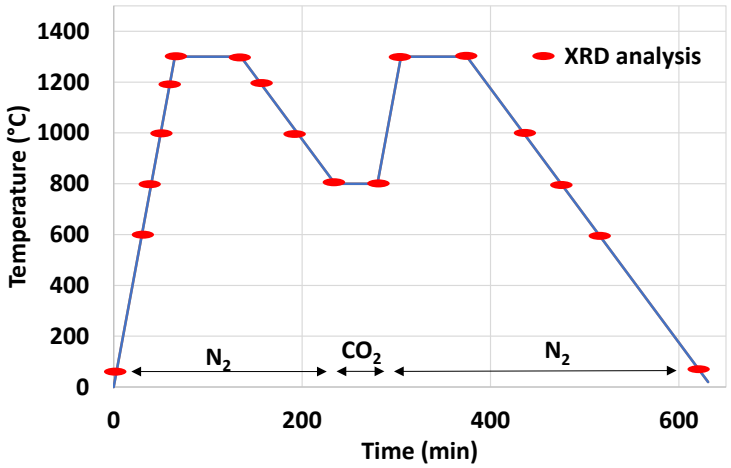

Figure 14. Temperature profile for XRD in situ analysis.

Chemical elementary cartography was realized by energy dispersive X-ray spectroscopy (EDS) analysis to both estimate the chemical composition and observe the cations distribution (surface mapping) in the material. Analyses were performed using a Zeiss Sigma 300. The accelerating voltage was 15 keV. All these characterizations allowed to validate the synthesis of HEO with a single crystallographic structure and a randomized cationic distribution.

3.3. Reactivity Testing during Thermochemical Cycles

Metal oxide redox pairs are intended to be used ultimately in a solar reactor for CO_2/H_2O splitting to produce CO/H_2. In such a device, the material is placed in a cavity receiver (e.g., as powder or foam) in which the concentrated solar beams are focussed at the reactor aperture [19]. Because of technological concerns (reactor design and high-temperature materials' resistance and stability), the maximum temperature should not exceed approximately 1400–1500 °C. In a typical solar thermochemical cycle, the oxide is heated up to ~1400 °C under argon flow (reduction) and then cooled down at below 1100 °C with H_2O or CO_2 injection for the splitting step (temperature-swing cycle). Several successive cycles must be operated during a day, which implies that the redox materials' microstructure and morphology have to be stable to warrant a repeatable thermochemical

performance (i.e., no reactivity decrease during the cycling and fast kinetics during the splitting step). To investigate the materials' activity under representative conditions comparable to those found in solar experimental reactors, a thermogravimetric analysis was carried out using similar temperatures and atmosphere compositions.

Once the powders were fully characterized, their thermochemical activity during two-step CO_2-splitting cycles was investigated. The thermogravimetric analysis (TGA) was used to measure the mass variations (amount of oxygen exchanged) associated with the reduction and the oxidation steps of thermochemical cycles. TGA was performed using a SETARAM Setsys Evo 1750 apparatus in a controlled atmosphere. Approximately 100 mg of material (exact mass determined with a high precision balance) was introduced in a platinum crucible hung to the microbalance with platinum suspensions and placed inside the furnace chamber. Then, residual air in the furnace chamber was eliminated by preliminary pumping to operate in an inert atmosphere and to improve the reduction yield thanks to the low oxygen partial pressure. The sample was heated in argon flow (20 mL/min) at a heating rate of 20 °C/min up to the selected temperature set-point and the mass variation was registered continuously. The successive steps of the thermochemical cycles were realized at different temperatures (typically 1400 °C or 1300 °C dwelled for 45 min during the reduction step and 1050 °C dwelled for one hour during the CO_2-splitting step) and CO_2 was injected during the oxidation step (50% CO_2 in Ar with a CO_2 flowrate of 10 mL/min). The mass variations associated with the temperature-programmed cycles correspond to the oxygen release during reduction and the oxygen uptake during CO_2-splitting, which allow the calculation of both the reduction yield and the CO production yield.

4. Conclusions

High entropy oxides (HEOs) open a new route for renewable synthetic fuel production through solar-driven thermochemical cycles. This study compares the thermochemical performance and behavior of a series of HEO formulations used as redox catalysts during two-step redox cycles. Different formulations of HEO were synthesized and characterized based on various structural configurations and cationic substitutions in the crystal lattice of the materials. Furthermore, their redox activity was investigated by focusing on their ability to perform CO_2 splitting during thermochemical cycles while quantifying the fuel production yields, rates and performance stability. Compared to previous values reported in the literature, HEO 1 and HEO 2 related to iron oxides do not exhibit an equivalent performance but they offer fuel production yields higher than those of ceria under similar conditions. Other HEO formulations were considered in this work and tested for the first time for thermochemical cycles application. Unfortunately, relatively small amounts of CO were produced per cycle for the other tested materials and experimental conditions. The ceria-related high entropy oxide (HEO 3) and the ferrite-related high entropy oxide (HEO 7) do not produce CO during thermochemical cycling, while the high entropy perovskites (HEOs 4, 5, and 6) do not exhibit higher performances than LSMMg. The HEO phase formation is strongly dependent on the heating rate or quenching. The reversible multi-phase to single-phase change could be integrated in a redox cycle and the high entropy variation between the different steps could permit the decrease in the working temperatures. The wide compositional space offered by HEO enables the design of new redox-active materials devoted to H_2O- or CO_2-splitting cycles using concentrated solar energy and should lead to abundant and high-impact research in this field.

Author Contributions: Conceptualization, A.L.G. and S.A.; methodology, A.L.G. and S.A.; validation, S.A. and A.J.; investigation, A.L.G., S.A. and M.V.; data curation, A.L.G.; writing—original draft preparation, A.L.G.; writing—review and editing, A.L.G., S.A. and A.J.; supervision, S.A. and A.J.; project administration, S.A.; funding acquisition, S.A. All authors have read and agreed to the published version of the manuscript.

Funding: This research was funded by the H2VERT project led by Région Occitanie in France (Défi clé Hydrogène Vert-Plan de relance-FEDER REACT EU-Hydrosol sub-project).

Data Availability Statement: The data presented in this study are available on request from the corresponding author.

Acknowledgments: The authors acknowledge support from E. Bêche from the PCM characterization platform in PROMES-CNRS during the XRD analysis; B. Rebière from the microscopy platform at IEM during EDS analysis and B. Fraisse from the analysis and characterization platform of the Pole Chimie Balard for the temperature-programmed XRD analysis.

Conflicts of Interest: The authors declare no conflict of interest. The funders had no role in the design of the study; in the collection, analyses, or interpretation of data; in the writing of the manuscript; or in the decision to publish the results.

References

1. Erbach, G.; Jensen, L. EU Hydrogen Policy, Hydrogen as an Energy Carrier for a Climate-Neutral Economy, European Parliamentary Research Service. Available online: https://www.europarl.europa.eu/RegData/etudes/BRIE/2021/689332/EPRS_BRI(2021)689332_EN.pdf (accessed on 1 July 2022)
2. US Department of Energy. Hydrogen Energy Earthshot. Available online: https://www.energy.gov/eere/fuelcells/hydrogenshot (accessed on 1 July 2022**.**
3. Japanese Ministerial Council on Renewable Energy, Hydrogen and Related Issues, Basic Hydrogen Strategy. Available online: https://www.meti.go.jp/english/press/2017/pdf/1226_003b.pdf (accessed on 1 July 2022).
4. Funk, J.; Reinstrom, R. Energy requirements in the production of hydrogen from water. *Ind. Eng. Chem. Process Des. Dev.* **1966**, *5*, 336–342.
5. Schäppi, R.; Rutz, D.; Dähler, F.; Muroyama, A.; Haueter, P.; Lilliestam, J.; Patt, A.; Furler, P.; Steinfeld, A. Drop-in fuels from sunlight and air. *Nature* **2021**, *601*, 63–68.
6. Zoller, S.; Koepf, E.; Nizamian, D.; Stephan, M.; Patane, A.; Haueter, P.; Romero, M.; Gonzalez-Aguilar, J.; Lieftink, D.; de Wit, E.; et al. A solar tower fuel plant for the thermochemical production of kerosene from H_2O and CO_2. *Joule* **2022**, *6*, 1606–1616.
7. Ma, Z.; Davenport, P.; Saur, G. System and technoeconomic analysis of solar thermochemical hydrogen production. *Renew. Energy* **2022**, *190*, 294–308.
8. Falter, C.; Valente, A.; Habersetzer, A.; Iribarren, D.; Dufour, J. An integrated techno-economic, environmental and social assessment of the solar thermochemical fuel pathway. *Sustain. Energy Fuels* **2020**, *4*, 3992–4002.
9. Kodama, T.; Gokon, N.; Yamamoto, R. Thermochemical two-step water-splitting by ZrO_2-supported $Ni_xFe_{2-x}O_4$ for solar hydrogen production. *Sol. Energy* **2008**, *82*, 73–79.
10. Gokon, N.; Murayama, H.; Nagasaki, A.; Kodama, T. Thermochemical two-step water-splitting cycles by monoclinic ZrO_2-supported $NiFe_2O_4$ and Fe_3O_4 powders and ceramic foam devices. *Sol. Energy* **2009**, *89*, 527–537.
11. Gokon, N.; Takahashi, S.; Yamamoto, H.; Kodama, T. Thermochemical two-step water-splitting reactor with internally circulating fluidized bed for thermal reduction of ferrites particles. *Int. J. Hydrogen Energy* **2008**, *33*, 2189–2199.
12. Allendorf, M.; Diver, R.; Siegel, N.; Miller, J. Two-step water splitting using mixed metal ferrites: Thermodynamic analysis and characterization of synthesized materials. *Energy Fuels* **2008**, *22*, 4115–4124.
13. Abanades, S.; Flamant, G. Thermochemical hydrogen production from a two-step solar-driven water splitting cycle based on cerium oxides. *Sol. Energy* **2006**, *80*, 1611–1623.
14. Chueh, W.; Haile, S. A thermochemical study of ceria: Exploiting an old material for new modes of energy conversion and CO_2 mitigation. *Philos. Trans. R. Soc. A* **2010**, *368*, 3269–3294.
15. Le Gal, A.; Abanades, S.; Flamant, G. CO_2 and H_2O splitting for thermochemical production of solar fuels using non-stoichiometric ceria and ceria/zirconia solid solutions. *Energy Fuels* **2011**, *25*, 4836–4845.
16. Furler, P.; Scheffe, J.; Steinfeld, A. Syngas production by simultaneous splitting of H_2O and CO_2 via ceria redox reactions in a high-temperature solar reactor. *Energy Environ. Sci.* **2012**, *5*, 6098–6103.
17. Furler, P.; Scheffe, J.; Gorbar, M.; Moes, L.; Vogt, U.; Steinfeld, A. Solar thermochemical CO_2 splitting utilizing a reticulated porous ceria redox system. *Energy Fuels* **2012**, *26*, 7051–7059.
18. Haeussler, A.; Abanades, S.; Jouannaux, J.; Drobek, M.; Ayral, A.; Julbe, A. Recent progress on ceria doping and shaping strategies for solar thermochemical water and CO_2 splitting cycles. *AIMS Mater. Sci.* **2019**, *6*, 657–684.
19. Haeussler, A.; Abanades, S.; Julbe, A.; Jouannaux, J.; Drobek, M.; Ayral, A.; Cartoixa, B. Remarkable performance of microstructured ceria foams for thermochemical splitting of H_2O and CO_2 in a novel high-temperature solar reactor. *Chem. Eng. Res. Des.* **2020**, *156*, 311–323.
20. Haeussler, A.; Abanades, S.; Jouannaux, J.; Julbe, A. Demonstration of a ceria membrane solar reactor promoted by dual perovskite coatings for continuous and isothermal redox splitting of CO_2 and H_2O. *J. Membr. Sci.* **2021**, *634*, 119387.

21. Haeussler, A.; Abanades, S. Additive manufacturing and two-step redox cycling of ordered porous ceria structures for solar-driven thermochemical fuel production. *Chem. Eng. Sci.* **2021**, *246*, 116999.
22. Scheffe, J.; Weibel, D.; Steinfeld, A. Lanthanum-strontium-manganese perovskites as redox materials for solar thermochemical splitting of H_2O and CO_2. *Energy Fuels* **2013**, *27*, 4250−4257.
23. Demont, A.; Abanades, S.; Beche, E. Investigation of perovskite structures as oxygen-exchange redox materials for hydrogen production from thermochemical two-step water splitting cycles. *J. Phys. Chem. C* **2014**, *118*, 12682–12692.
24. Orfila, M.; Linares, M.; Molina, R.; Botas, J.; Sanz, R.; Marugan, J. Perovskite materials for hydrogen production by thermochemical water splitting. *Int. J. Hydrogen Energy* **2016**, *41*, 19329–19338.
25. Haeussler, A.; Abanades, S.; Jouannaux, J.; Julbe, A. Non-stoichiometric redox active perovskite materials for solar thermochemical fuel production: A review. *Catalysts* **2018**, *8*, 611.
26. Nair, M.; Abanades, S. Insights into the redox performance of non-stoichiometric lanthanum Manganite Perovskites for Solar Thermochemical CO_2 Splitting. *ChemistrySelect* **2016**, *1*, 4449–4457.
27. Nair, M.M.; Abanades, S. Experimental screening of perovskite oxides as efficient redox materials for solar thermochemical CO2 conversion. *Sustain. Energy Fuels* **2018**, *2*, 843–854.
28. Haeussler, A.; Julbe, A.; Abanades, S. Investigation of reactive perovskite materials for solar fuel production via two-step redox cycles: Thermochemical activity, thermodynamic properties and reduction kinetics. *Mater. Chem. Phys.* **2022**, *276*, 125358.
29. Lorentzou, S.; Zygogianni, A.; Pagkoura, C.; Karagiannakis, G.; Konstandopoulos, A.G.; Saeck, J.P.; Breuer, S.; Lange, M.; Lapp, J.; Fend, T.; et al. HYDROSOL-PLANT: Structured redox reactors for H_2 production from solar thermochemical H_2O splitting. *AIP Conf. Proc.* **2018**, *2033*, 130010.
30. **Lu, Y.; Zhu, L.; Agrafiotis, C.; Vieten, J.; Roeb, M.; Sattler, C. Solar fuel production: Two-step thermochemical cycles with cerium-based oxides. *Prog. Energy Combust. Sci.* 2019, *75*, 100785.**
31. Marxer, D.; Furler, P.; Takacs, M.; Steinfeld, A. Solar thermochemical splitting of CO_2 into separate streams of CO and O_2 with high selectivity, stability, conversion, and efficiency. *Energy Environ. Sci.* **2017**, *10*, 1142–1149.
32. Yang, C.; Yamazaki, Y.; Aydin, A.; Haile, S. Thermodynamic and kinetic assessment of strontium-doped lanthanum manganite perovskites for two-step thermochemical water splitting. *J. Mater. Chem*. **2014**, *2*, 13612–13623.
33. Kim, Y.; Jeong, S.; Koo, B.; Lee, S.; Kwak, N.; Jung, W. Study of the surface reaction kinetics of (La,Sr)MnO3 oxygen carriers for solar thermochemical fuel production. *J. Mater. Chem*. **2018**, *6*, 13082–13089.
34. Bulfin, B.; Vieten, J.; Agrafiotis, C.; Roeb, M.; Sattler, C. Applications and limitations of two-step metal oxide thermochemical redox cycles: A review. *J. Mater. Chem A* **2017**, *5*, 18951–18966.
35. Mao, Y.; Gao, Y.; Dong, W.; Wu, H.; Song, H.; Zhao, X.; Sun, J.; Wang, W. Hydrogen production via two-step water splitting thermochemical cycle based on metal oxide—A review. *Appl. Energy* **2020**, *267*, 114860.
36. Abanades, S. Metal oxides applied to thermochemical water-splitting for hydrogen production using concentrated solar energy. *Chem Eng.* **2019**, *3*, 63.
37. Rost, C.M.; Sachet, E.; Borman, T.; Moballegh, A.; Dickey, E.; Hou, D.; Jones, J.; Curtarolo, S.; Maria, J.-P. Entropy-stabilized oxides. *Nat. Commun.* **2015**, *6*, 8485.
38. Berdaran, D.; Meena, A.; Franger, S.; Dragoe, N. Room temperature lithium superionic conductivity in high entropy oxides. *J. Mater. Chem. A* **2016**, *4*, 9536–9541.
39. Berdaran, D.; Franger, S.; Meena, A.; Dragoe, N. Colossal dielectric constant in high entropy oxides. *Phys. Status Solidi* **2016**, *10*, 328–333.
40. Breitung, B.; Wang, Q.; Schiele, A.; Tripkovic, D.; Sarkar, A.; Velasco, L.; Wang, D.; Bhattacharya, S.; Hahn, H.; Brezesinski, T. Gassing behavior of high entropy oxide anode and oxyfluoride cathode probed using differential electrochemical mass spectroscopy. *Battery Supercaps* **2020**, *3*, 361–369.
41. Sarkar, A.; Loho, C.; Velasco, L.; Thomas, T.; Bhattacharya, S.; Hahn, H.; Djenadic, R. Multicomponent equiatomic rare earth oxides with a narrow band gap and associated praseodymium multivalency. *Dalton Trans.* **2017**, *46*, 12167–12176.
42. Sarkar, A.; Eggert, B.; Velasco, L.; Mu, X.; Lill, J.; Ollefs, K.; Bhattacharya, S.; Wende, H.; Kruk, R.; Brand, R.; et al. Role of intermediate 4f states in tuning the band structure of high entropy oxides. *APL Mater.* **2020**, *8*, 051111.
43. Braun, J.; Rost, C.; Lim, M.; Giri, A.; Olson, D.; Kotsonis, G.; Stan, G.; Brenner, D.; Maria, J.; Hopkins, P. Charge-induced disorder controls the thermal conductivity of entropy stabilized oxides. *Adv. Mater.* **2018**, *30*, e1805004.
44. Wang, D.; Liu, Z.; Zhang, Y.; Li, H.; Xiao, Z.; Chen, W.; Chen, R.; Wang, Y.; Zou, Y.; Wang, S. Low temperature synthesis of small sized high entropy oxides for water oxidation. *J. Mater. Chem. A* **2019**, *7*, 24211–24216.
45. Zhai, S.; Rojas, J.; Ahlborg, N.; Lim, K.; Toney, M.; Jin, H.; Chueh, W.; Majumdar, A. The use of poly-cation oxides to lower the temperature of two-step thermochemical water splitting. *Energy Environ. Sci.* **2018**, *11*, 2172–2178.
46. Gao, Y.; Mao, Y.; Song, Z.; Zhao, X.; Sun, J.; Wang, W.; Chen, G.; Chen, S. Efficient generation of hydrogen by two-step thermochemical cycles: Successive thermal reduction and water splitting reactions using equal-power microwave irradiation and a high entropy material. *Appl. Energy* **2020**, *279*, 115777.

47. Gao, Y.; Zhang, M.; Mao, Y.; Cao, H.; Zhang, S.; Wang, W.; Sun, C.; Song, Z.; Sun, J.; Zhao, X. Microwave-triggered low temperature thermal reduction of Zr-modified high entropy oxides with extraordinary thermochemical H2 production performance. *Energy Convers. Manag.* **2022**, *252*, 115125.
48. Pianassola, M.; Loveday, M.; McMurray, J.; Koschan, M.; Melcher, C.; Zhuravleva, M. Solid state synthesis of multicomponent equiatomic rare-earth oxides. *J. Am. Ceram. Soc.* **2020**, *103*, 2908–2918.
49. Djenadic, R.; Sarkar, A.; Clemens, O.; Loho, C.; Botros, M.; Chakravadhanula, V.; Kubel, C.; Bhattacharya, S.; Gandhi, A.; Hahn, H. Multicomponent equiatomic rare earth oxides. *Mater. Res. Lett.* **2017**, *5*, 102–109.
50. Sarkar, A.; Djenadic, R.; Wang, D.; Hein, C.; Kautenburger, R.; Clemens, O.; Hahn, H. Rare earth and transition metal based entropy stabilised perovskite type oxides. *J. Eur. Ceram. Soc.* **2018**, *38*, 2318–2327.
51. De Santiago, H.A.; Zhang, D.; Park, J.; Li, W.; McDaniel, A.; Coker, E.; Sugar, J.; Lany, S.; Qi, Y.; Luo, J. A new class of high entropy oxides with increased reducibility and stability for solar thermochemical hydrogen production. *ECS Meet. Abstr.* **2021**, *MA2021-02*, 1354.
52. Biesuz, M.; Spiridigliozzi, L.; Dell'Agli, G.; Bortolotti, M.; Sglavo, V. Synthesis and sintering of (Mg,Co,Ni,Cu,Zn)O entropy-stabilized oxides obtained by wet chemichal method. *J. Mater. Sci.* **2018**, *53*, 8074–8085.
53. Gangavarapu, R.; Ali, M.; Roychowdhury, S.; Prasad, L. Promising oxygen storage capacity of equimolar high entropy transition metal oxide (MgCoNiCuZn)O. *Mater. Lett.* **2021**, *304*, 130635.
54. Musico, B.; Wright, Q.; Ward, Z.; Grutter, A.; Arenholz, E.; Gilbert, D.; Mandrus, D.; Keppens, V. Tunable magnetic ordering through cation selection in entropic spinel oxides. *Phys. Rev. Mater.* **2019**, *3*, 104416.
55. Charvin, P.; Abanades, S.; Bêche, E.; Lemont, F.; Flamant, G. Hydrogen production from mixed cerium oxides via three-step water-splitting cycles. *Solid State Ion.* **2009**, *180*, 1003–1010.
56. Sunde, T.; Grande, T.; Einarsrud, M. Modified Pechini synthesis of oxide powders and thin films. In *Handbook of Sol-Gel Science and Technology*; Klein, L., Aparicio, M., Jitianu, A., Eds. Springer International Publishing; Cham, Switzerland; 2018; pp. 1089–1118.